Made available through Montana State University's ScholarWorks

Satellite detection of snow avalanches using Sentinel-1 in a transitional snow climate

Zachary Keskinen, Jordy Hendrikx, Markus Eckerstorfer, Karl Birkeland

© This manuscript version is made available under the CC-BY-NC-ND 4.0 license https://creativecommons.org/licenses/by-nc-nd/4.0/

Satellite Detection of Snow Avalanches using Sentinel-1 in a Transitional Snow Climate

Zachary Keskinen*[1,2], Jordy Hendrikx[1], Markus Eckerstorfer[3,4], Karl Birkeland[5,1]

[1] Snow and Avalanche Lab, Department of Earth Sciences, Montana State University, P.O Box 173480, Bozeman, MT, 59717, USA

[2] Cryogars, Department of Geoscience, Boise State University, 1295 University Drive, Boise, ID, 83706, USA

[3] Regional Climate Lab., Climate Department, NORCE Norwegian Research Centre, N-5838 Bergen, Norway

[4] Bjerknes Centre for Climate Research, N-5007 Bergen, Norway

[5] U.S.D.A. Forest Service National Avalanche Center, Bozeman, MT, USA

* Corresponding Author: 940 Snowflake Dr., Hailey ID 83333. Zachkeskinen@gmail.com

Snow avalanches endanger lives and infrastructure in mountainous regions worldwide. Consistent and accurate datasets of avalanche events are critical for improving hazard forecasting and understanding the spatial and temporal patterns of avalanche activity. Remote sensing-based identification of avalanche debris allow for the acquisition of continuous and spatially consistent avalanches datasets. This study utilizes expert manual interpretations of Sentinel-1 synthetic aperture radar (SAR) satellite backscatter images to identify avalanche debris and compares

those detections against historical field records of observed avalanches in the transitional snow climates of Wyoming and Utah, USA. We explore and quantify the ability of an expert using Sentinel-1 (a SAR satellite) images to detect avalanche debris on a dataset comprised exclusively of dry slab avalanches. This research utilized four avalanche cycles with 258 field reported avalanches. Due to individual avalanches appearing in multiple overlapping Sentinel-1 images this resulted in 506 potential detections of avalanches in our SAR images, representing the possibility of multiple detections of a single avalanche event in different images. The overall probability of detection (POD) for avalanches large enough to destroy trees or bury a car (i.e., ≥D3 on the destructive size scale) was 65%. There was a significant variance in the POD among the 13 individual SAR image pairs considered (15 – 86%). Additionally, this study investigated the connection between successful avalanche detections and SAR-specific, topographic, and avalanche type variables. The most correlated variables with higher detection rates were avalanche path lengths, destructive size of the avalanche, incidence angles for the incoming microwaves, average path slope angle, and elapsed time between the avalanche and a Sentinel-1 satellite image acquisition. This study provides a quantification of the controlling variables in the likelihood of detecting avalanches using Sentinel-1 backscatter temporal change detection techniques, as specifically applied to a transitional snow climate.

Keywords: Remote Sensing, Snow avalanches, Terrain, Synthetic Aperture Radar

Highlights:

- Dry slab avalanches ≥D3 had a detection rate of 65%;

- Improved quantification of controlling variables on SAR based avalanche detection;
- Path length, D size, and average slope correlated with higher detections;
- Incidence angle and time between event and image acquisition also correlated with higher detections;

1 Introduction

Snow avalanches are a complex mountain hazard that endangers lives, threatens infrastructure, and closes transportation corridors (e.g. McClung and Schaerer 2006, Hendrikx et al., 2014, Birkeland et al., 2017). Timely knowledge about when and where avalanches occur is vital for avalanche risk assessment and forecasting (McClung, 2002a, 2002b). Currently, gathering data about the spatial distribution and magnitude of avalanche events most typically relies on human field observers and is consequently spatially and temporally limited. Other sources of avalanche records, such as airborne surveys or infrasound arrays, are cost prohibitive to implement consistently over large regions. However, human observations rarely cover an entire mountain range, are limited by low visibility or high danger conditions, and are biased towards accessible locations and convenient collection periods (Eckerstorfer and Malnes, 2015).

Recent research has shown promising results from radar satellite-based avalanche detections as an alternative method to provide near real-time, consistent data about avalanche occurrences (Eckerstorfer et al., 2019; Leinss et al., 2020). Radar satellite-based detections provide a valuable supplement to field-based observations due to their large spatial coverage and the temporal consistency with which avalanches can be observed, allowing for more reliable comparisons of

avalanche activity. A sensor that has demonstrated specific utility in detecting avalanche debris is Synthetic Aperture Radar (SAR) (Eckerstorfer et al., 2016; Leinss et al., 2020; Yang et al., 2020). SAR sensors emit energy in the microwave spectrum (wavelengths of 1 – 300 mm) which are not affected by cloud cover or darkness, allowing for temporally and spatially consistent remote sensing.

SAR-equipped satellites have been used to detect avalanche debris since the early 2000s (Wiesmann et al., 2001). However, the recent introduction of freely available imagery from the Sentinel-1 SAR satellite constellation has vastly expanded opportunities for SAR-borne avalanche detection. Multiple studies exploited Sentinel-1 imagery to map avalanche cycles and create automatic detection systems (Abermann et al., 2019; Eckerstorfer et al., 2019; Leinss et al., 2020). Eckerstorfer et al. (2019), working in a maritime snow climate, provided one of the few studies comparing manual detections using SAR backscatter change detection against avalanche field observations. Their study compared field-observed datasets of avalanche activity against manual interpretations of SAR images and automated detections. They reported an overall probability of detection (POD) of 77.3%. Multiple factors, however, influenced the overall detectability of avalanches. Large avalanches resulted in a 100% POD and were more detectable than small avalanches (64.9%), as a consequence the spatial resolution of the Sentinel-1 SAR sensor. Wet snow avalanches were more detectable than dry snow avalanches due to higher relative backscatter from rougher wet snow avalanche debris. Leinss et al. (2020) provided an important first exploration of the utility of Sentinel-1 in detecting avalanches in a transitional snow climate in Switzerland during a major avalanche cycle from January 2018. However, they did not quantify the accuracy of Sentinel-1 borne avalanche detections due to a

lack of field-based validation data. They manually delineated 104 avalanches in Sentinel-1 data compared to 164 in higher resolution TerraSAR-X data. They suggested a minimum detectable Sentinel-1 avalanche debris size of 2000 m^2. They, moreover, noted that avalanches that descended "below the wet-snow line were much more visible than avalanches from the dry snow-zone", suggesting that dry slab avalanches may be harder to detect. Finally, they suggested that higher incidence angles should provide higher detection rates, but did not test this theory directly. More recent research has explored this relationship between incidence angle and increased backscatter. Tompkin and Leinss (2021), exploring a dataset of exclusively wet snow avalanches, found that, compared to an optimal incidence angle of ~55°, backscatter was reduced by 4 dB for incidence angles below 40° in VV polarization (vertically transmitted and received signal). They also found that backscatter intensity also decreased for incidence angles over 70 degrees. This study showed the importance of incidence angles and the utility of local resolution weighting that prioritizes higher incidence angles in multi-image composites. However, more research is necessary to confirm this relationship in other snow conditions and study sites. Building on the avalanche detections in Switzerland, Hafner et al. (2021) detected avalanches using Sentinel-1 and the optical Sentinel-2 and SPOT-6. Using Sentinel-1 imagery they were able to detect 90% of avalanches large enough to destroy substantial forest, but only 4% of those harmless to people. Conversely to other studies Hafner et al. (2021) found higher detection rates for the dry-snow conditions relative to the mixed wet and snow avalanche cycle. The suggested that in scene-wide dry-snow only conditions the "avalanches were the most prominent changes in the backscatter signal". The larger scene-wide backscatter changes in wet to dry snow conditions could make detections more challenging.

While backscatter change detection is valuable for detecting avalanche debris, important questions remain about the strengths and limitations of this technique. Without a thorough understanding of the benchmark avalanche detection rate and how it varies as a function of topographic and SAR-specific variables, we cannot accurately communicate the global utility of this technique or accurately assess the performance of automated detection systems. Therefore, the purpose of this study is to compare Sentinel-1 SAR manual detections to field-observations of exclusively dry slab avalanches in a transitional snow climate in two different regions of the western United States. We address the following questions:

1. What are the manual detection rates of dry slab avalanches using change detection techniques on Sentinel-1 SAR backscatter images in the transitional snow climates of Utah and Wyoming, U.S.A.?
2. How do topographic (elevation, path length, slope, curvature, tree coverage), SAR (incidence angle, layover, shadow, and days between images) and avalanche characteristics (destructive size) affect SAR avalanche detection rates?

2 Methods and datasets

To answer our research questions, we consider two primary sources: 1) field observations of avalanches, and 2) manual detections in Sentinel-1 data (Figure 1). For processing and analysis, we consider three ancillary data sources: Global Forest Cover Change Tree Cover (Sexton et al., 2013), USGS National Elevation Dataset (Gesch et al., 2002), and auto-Avalanche Terrain Exposure maps (Larsen et al., 2020) (Figure 1).

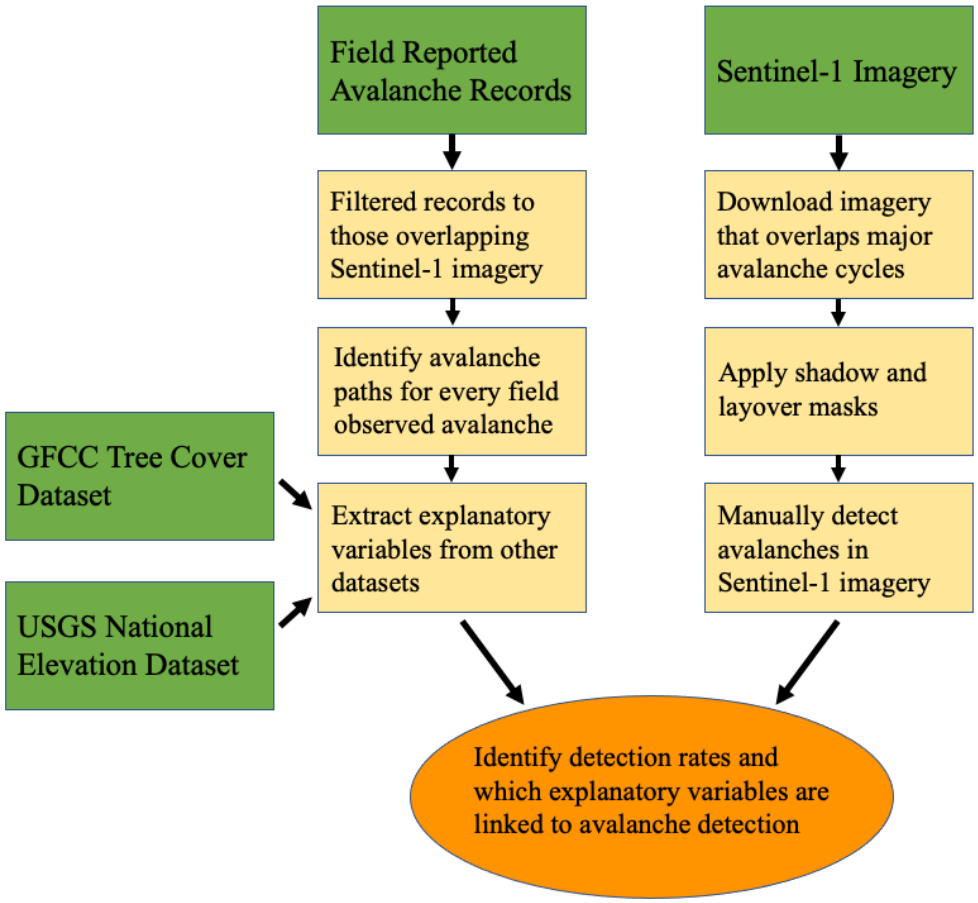

Figure 1: Flowchart of data collection and processing steps. Green shows input datasets, yellow shows processing and analysis steps, and orange shows statistical analysis steps.

2.1. Sentinel-1 datasets:

The Sentinel-1 constellation is a pair of polar-orbiting, sun-synchronous satellites with a 6-day orbit repeat interval. Due to overlapping image footprints between orbital geometries at higher latitude this image frequency can be as little as 1 day at higher latitudes. Both satellites are equipped with C-band SAR sensors (wavelength ~5.54 cm) that acquire SAR images with roughly 20 m pixel resolution in interferometric wide swath mode (IW) in both co-polarized (e.g. VV) and cross-polarized (e.g. VH) polarization.

We downloaded Sentinel-1 backscatter intensity images (ground range detection – GDR products) from Google Earth Engine (GEE) (Gorelick et al. 2017) that matched the timing of major avalanche cycles (see section below) and processed them as follows:

- Sentinel-1 imagery was preprocessed by GEE via the application of a precise orbit file, removal of border and thermal noise, application of radiometric calibration, and terrain correction (Gorelick et al., 2017).
- For each Sentinel-1 image, we created and applied layover and shadow masks using the United States Geological Survey's (USGS) National Elevation Dataset at 1/3 arc-second resolution (Gesch et al., 2002). During this step, we also extracted local incidence angles for each pixel. This processing workflow used a python script adapted from Vollrath et al. (2020) (please refer to the supplemental materials).

To visualize temporal backscatter intensity change necessary for manual avalanche detection, we paired Sentinel-1 images of same orbital geometry (ASC- ascending or DES – descending) and

159 track number (e.g. DES 100). Sentinel-1 image pairs contained a reference and an activity image.
160 For our study these are 12 or 24 days apart instead of 6 due to lower imaging frequency over
161 these areas in the ESA's operational plan.
162

163 ## 2.2 Field-observed avalanche datasets

164 We used records of field-observed avalanches in a transitional snow climate in the USA (Mock
165 and Birkeland, 2000), from the Utah Department of Transportation (UDOT) and the Bridger
166 Teton Avalanche Center (BTAC). The BTAC records covered their avalanche forecasting region
167 near Jackson, Wyoming. UDOT avalanches were from Little Cottonwood Canyon outside of Salt
168 Lake City, Utah (

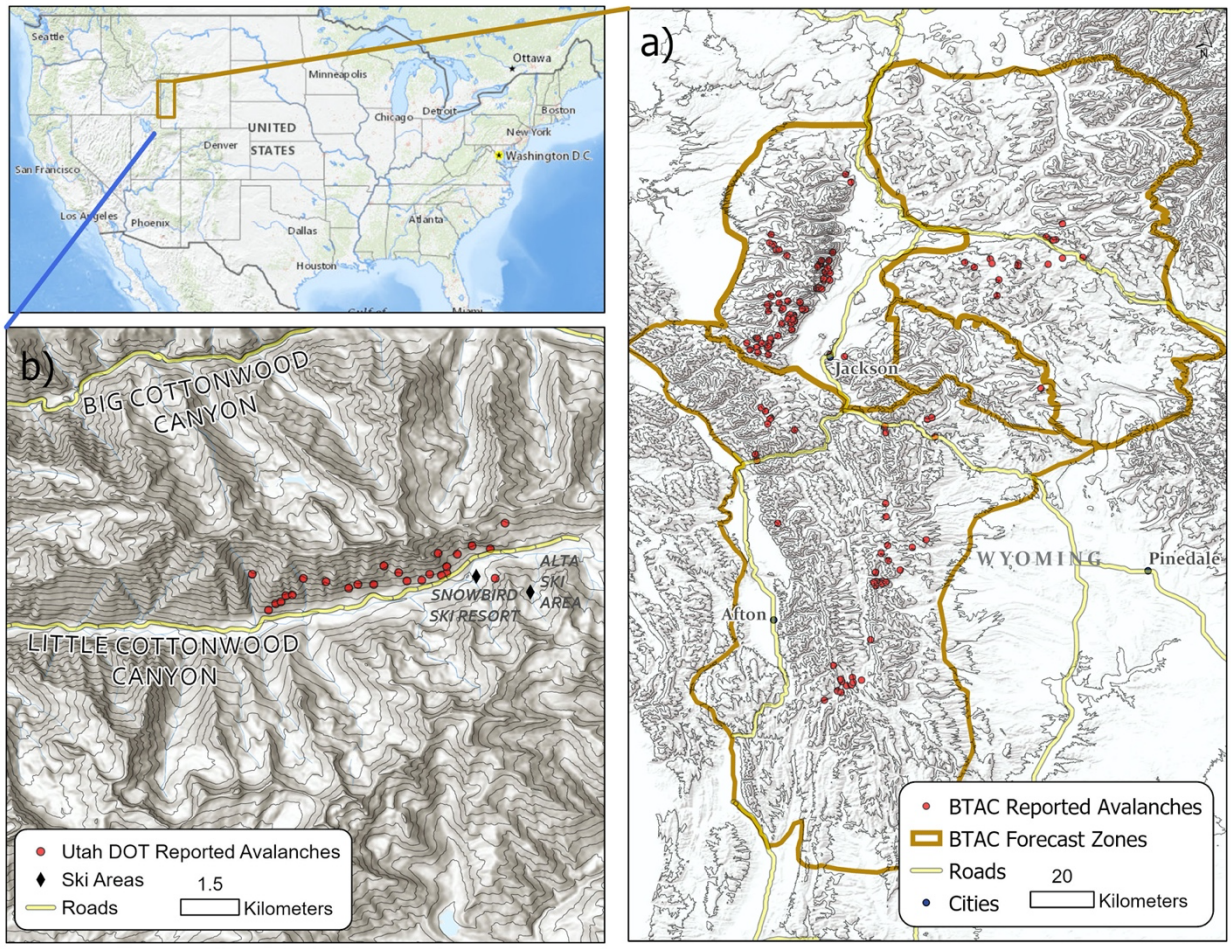

Figure 2).

These records included written descriptions of location, date, avalanche type, and destructive (D) size. The records were predominantly dry (88% for BTAC and 87% for UDOT) and slab (95% for BTAC and 85% for UDOT) avalanches. Slab avalanches result from the failure of an underlying weak layer and the release of a cohesive "slab" of snow, compared to loose avalanches where surface snow loses cohesion (Gaume et al., 2017). To focus our analysis exclusively on dry slab avalanches we filtered the records to only those avalanche types. We examined only avalanche records between 2016 –2020, covering the operational period for both satellites of the Sentinel-1 constellation.

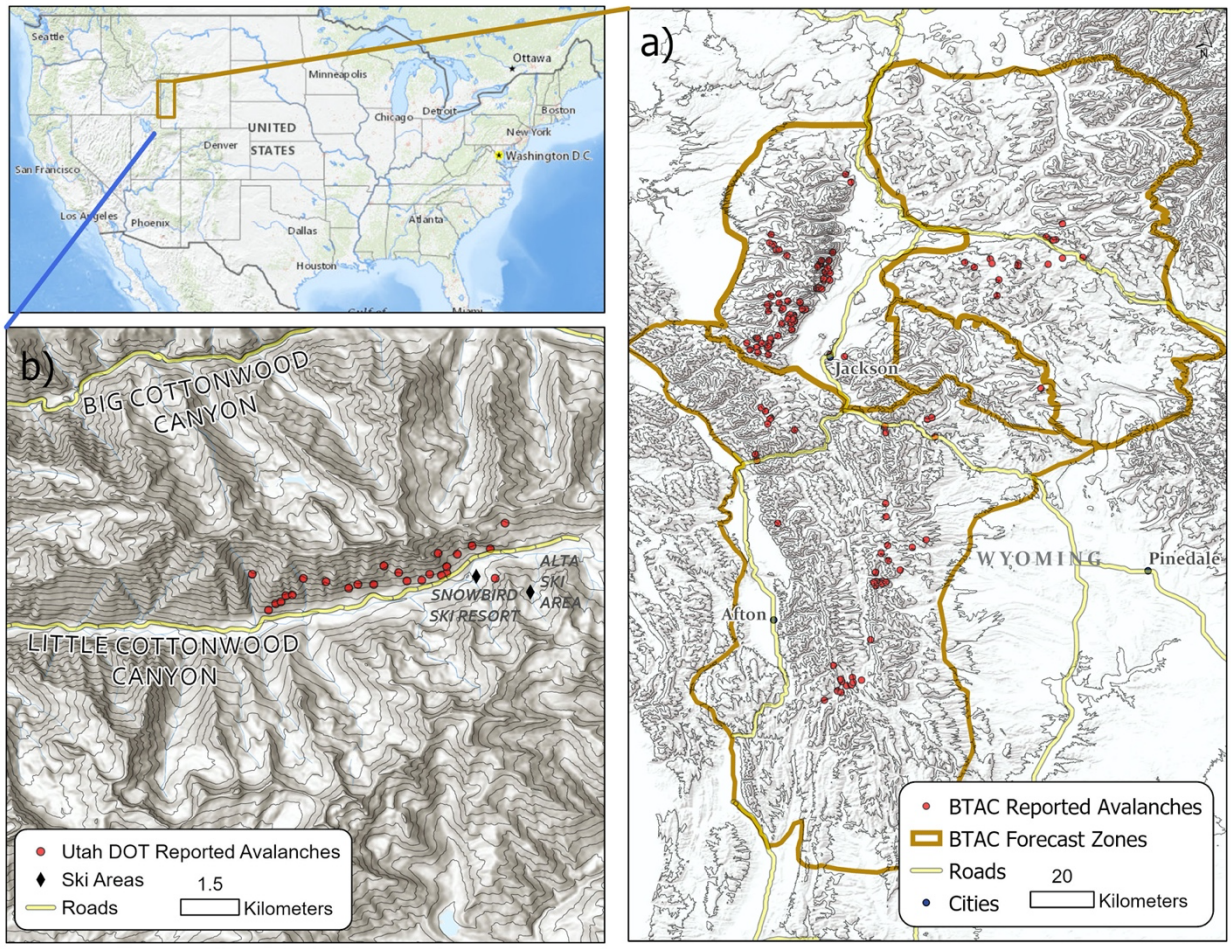

Figure 2: Avalanche locations for the a) BTAC (n = 134) and b) UDOT (n =124) avalanche databases.

We calculated avalanche activity indexes (AAIs) according to Schweizer et al. (2003) for each database to identify significant avalanche cycles. The AAI is the sum of observed avalanches weighted by their destructive size (D1: 0.01, D2: 0.1, D3:1, D4:10) for each day (Figure 3). Our study investigated the two most significant cycles using AAI scores from the BTAC (Figure 3(a): AAI = 120; (b): AAI = 41) and UDOT (Figure 3 (c): AAI = 80; (d): AAI = 111). These cycles' AAI scores exceed the 99th percentile for each respective dataset.

2.3 Comparison between Sentinel-1 avalanche detections and field-observed avalanche activity

We downloaded 14 Sentinel-1 image pairs. 7 image pairs spatially and temporally overlapped the BTAC avalanche cycles and 7 overlapped the UDOT avalanche cycles (Figure 3). The image pairs with matching orbital geometries and paths were all either 12, or 24 days apart.

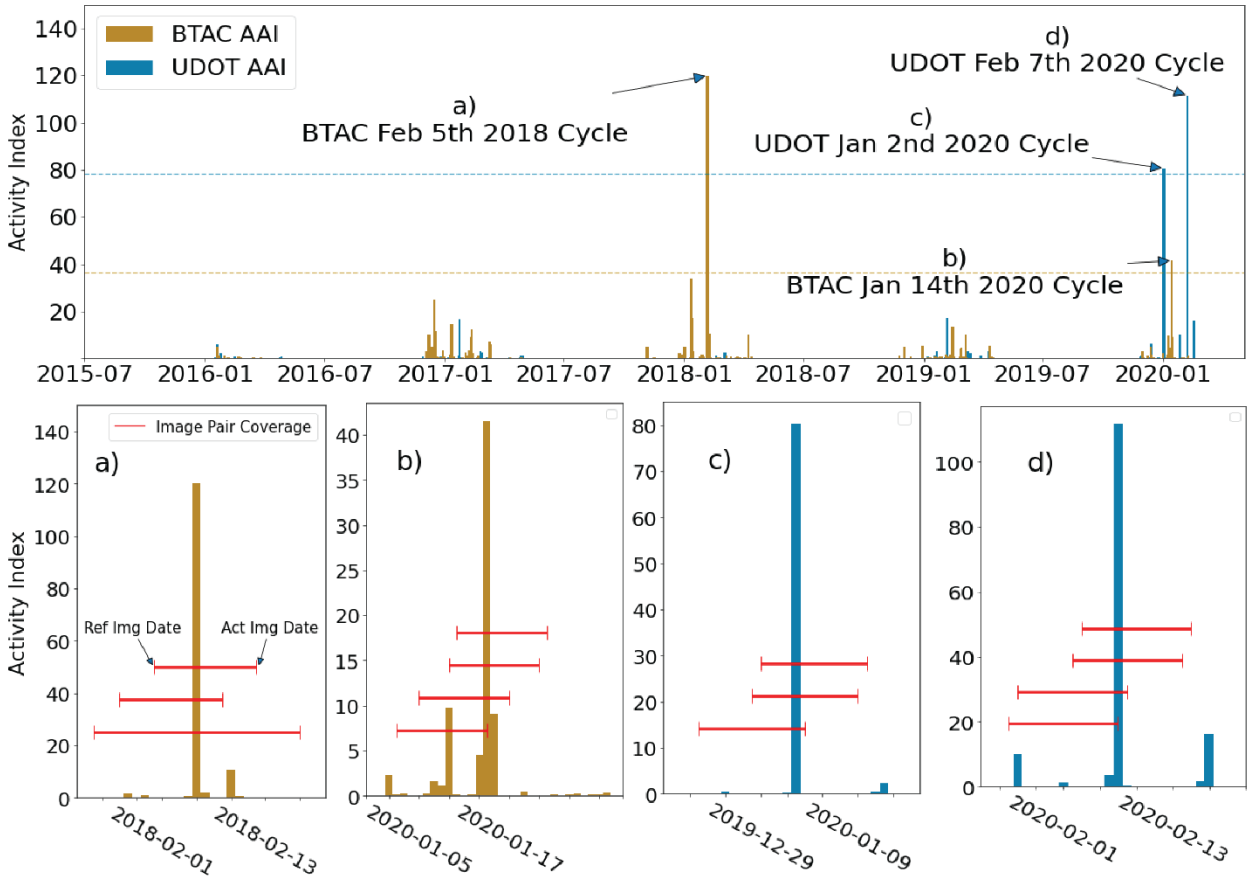

Figure 3: Avalanche activity index for the two databases from 2016-2020 with the two largest cycles for each region (four total) noted. The dashed lines show 99th percentile of the avalanche activity index for BTAC (AAI = 36) in beige, and UDOT (AAI = 78) in blue, showing the extreme nature of these events. Insets show each avalanche cycle with capped lines showing the imagery dates of all utilized Sentinel-1 image pairs. Note that insets a-d have different y-axes.

202

203 We analyzed all the avalanches that released between a reference and activity Sentinel-1 image.

204 In total, we used 7 descending and 7 ascending Sentinel-1 image pairs in this study (

Table 1). Within the time periods these Sentinel-1 image pairs covered, a total of 258 field reported avalanches were recorded in the two study regions. There were 124 UDOT avalanches. Of the UDOT avalanches, 23 (19%) were natural avalanches, and 101 (81%) were artificially triggered. For the BTAC dataset, there were 134 avalanches. Ninety-four were naturally triggered (69%), and 40 (31%) were artificially triggered. The destructive size distribution of both the UDOT and BTAC was centered on D2 (53%) and D3 (23%) (please refer to the supplementary material). Given the temporal overlap of the satellite orbits, these 258 field reported avalanches had the potential to be detected and counted in multiple pairs of images. This resulted in a final dataset of 506 potentially detectable avalanche events, representing multiple opportunities to count the 258 unique field observed events.

Table 1: Studied avalanche cycles from both study regions and orbit direction and satellite path number of the Sentinel-1 image pairs that match in space and time. The final column shows the total field reported avalanches that could have been detected in each pair of images. This number varies due to the varying spatial footprints and temporal coverage of each pair of images relative to the field reported avalanches and adds up to 506 total possible avalanche detections.

Activity Image Date	**Reference Image Date**	**Orbit Direction**	**Sat. Path #**	**Possible Avalanche Detections**
BTAC Feb. 5th, 2018 Cycle				
February 8th, 2018	January 27th, 2018	Ascending	49	31
February 12th, 2018	January 31st, 2018	Descending	27	43
February 17th, 2018 [1]	January 24th, 2018 [1]	Descending	100	19
BTAC Jan. 14th, 2020 Cycle				
January 14th, 2020	January 2nd, 2020	Descending	100	41
January 17th, 2020	January 5th, 2020	Ascending	49	28
January 21st, 2020	January 9th, 2020	Descending	27	41
January 22nd, 2020	January 10th, 2020	Ascending	122	40
UDOT Jan. 2nd, 2020 Cycle				
January 3rd, 2020	December 22nd, 2019	Ascending	20	44
January 9th, 2020	December 28th, 2019	Descending	27	18
January 10th, 2020	December 29th, 2019	Ascending	122	42
UDOT Feb. 7th, 2020 Cycle				
February 7th, 2020	January 26th, 2020	Descending	100	41
February 8th, 2020	January 27th, 2020	Ascending	20	45
February 14th, 2020	February 2nd, 2020	Descending	27	26
February 15th, 2020	February 3rd, 2020	Ascending	122	47

[1] *Only pair with 24 days instead of 12 days between imaging dates*

2.4 Avalanche path identification

Avalanche paths, defined here as the potential region affected by a 1 in 100-year avalanche from a specific start zone, were necessary to extract spatial averages of Sentinel-1 backscatter change and potential explanatory variables (Mears, 1992). For the UDOT region we used a pre-existing catalog of avalanche paths. An avalanche atlas was not available for the BTAC region.

Consequently, we delineated avalanche paths for each BTAC event based on the field recorded location, written descriptions and photographs of the avalanche and automatic Avalanche Terrain Exposure (auto-ATES) maps of the regions (Larsen et al. (2020). The starting zone and track were defined using the field description and photographs of the avalanche when available and otherwise following topographic constraining features (ridgelines). We drew the runout extent using auto-ATES maps to terminate the path at a 23-degree alpha angle from the starting zone (Larsen et al. 2020). These auto-ATES maps use alpha angles from the nearest starting zones to map potential avalanche hazard and were used to identify likely runout extent using the workflow in Larsen et al. (2020). We drew these avalanche paths before SAR debris detections to avoid biasing of the path characteristics.

2.5 Manual avalanche detection

To facilitate manual interpretation of the SAR images we created RGB composites, where we put the reference image in the red and blue channels and the activity image in the green channel (Figure 4). A temporal backscatter increase appears in green while a decrease appears in purple in these RGB composites. The RGB composites contained SAR images with the same geometry and path number, ensuring changing scattering properties resulted from changes in surface conditions and not from different incidence angles (Wynne and Campbell, 2011).
According to Eckerstorfer and Malnes (2015) avalanche debris exhibits higher backscatter than the surrounding undisturbed snow due to a higher contribution from the rougher surface-air interface, as well as some higher contribution from increased volumetric scattering within a thicker snowpack. Thus the occurrence of avalanche debris covering a pre-existing snowpack

leads to increase in backscatter that is visible as green, elongated features in the RGB composites (Figure 4) (Leinss et al., 2020; Malnes et al., 2013; Wiesmann et al., 2001). We examined all the RGB images for regions with increased backscatter within the marked avalanche paths. If these regions of localized backscatter increase matched the description and photos of the field-observed avalanches, and had at least a 2–3 decibels backscatter increase across the likely debris zone, then we marked them as ‘detected’. The UDOT dataset included multiple reported avalanches per avalanche path, while the BTAC dataset did not. These overlapping avalanches were either all marked "Detected" or "Not detected". The average avalanches per path in the UDOT dataset was 2.3.

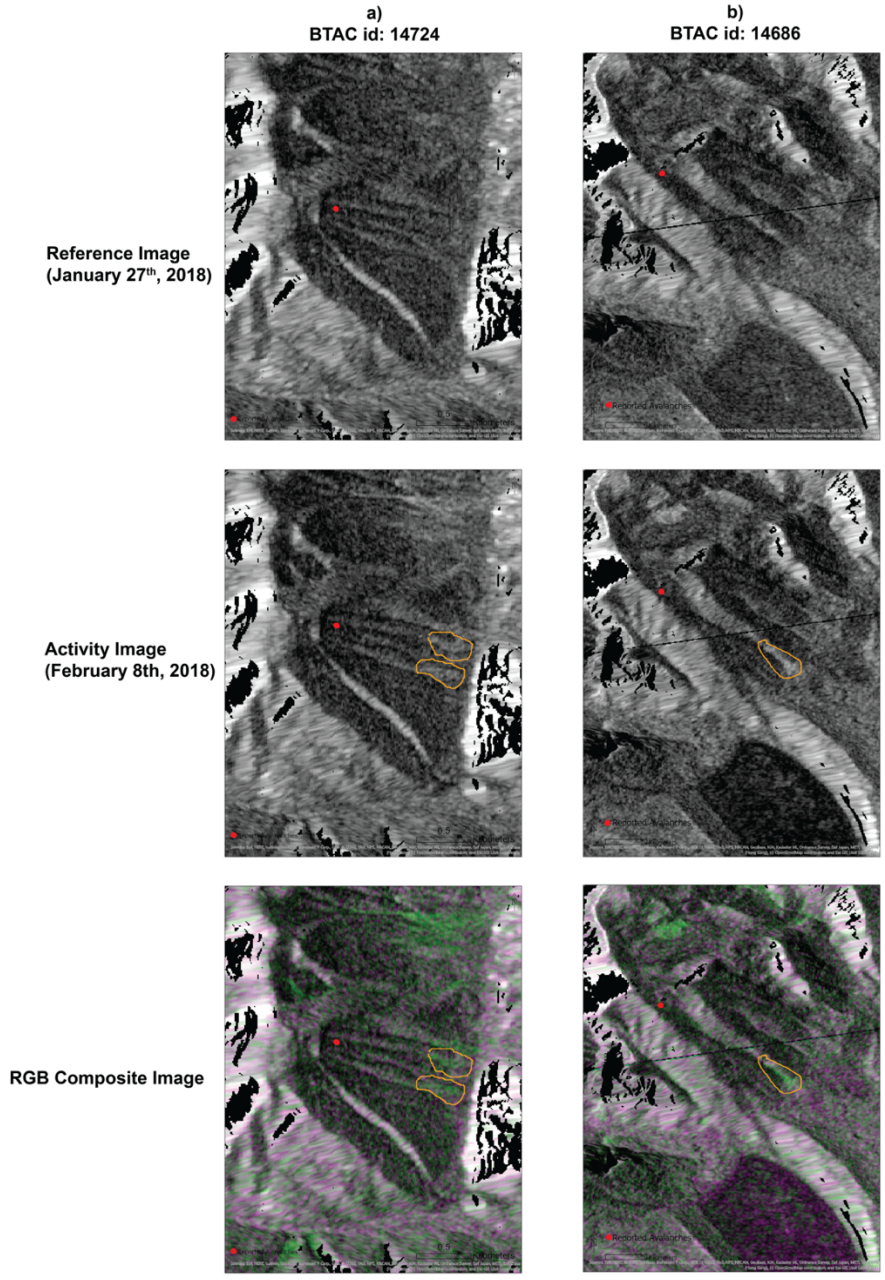

Figure 4: Reference, activity, and RGB composite images for (a) two and (b) one field reported avalanches in the BTAC region. Red dots show the field reported crown locations, polygons represent the manually detected debris outlines. Temporal change analysis compares the reference image to the activity image to identify increased backscatter areas. The diagonal black line across (b) is an artifact of merging two Sentinel-1 images into one. Other regions of significant increases in (a) and (b) are likely more avalanche debris that was not reported from the field due to their distance from roads or ski areas, though other possibilities include wind-drifted snow, ground roughness changes, and freezing or unfreezing of lakes or snow.

2.6 Explanatory variables for manual avalanche detection

We extracted possible explanatory variables for every recorded avalanche event, regardless of SAR detection. The avalanche databases from the BTAC and UDOT contained standard avalanche descriptive data, including dates, D-size, wet vs. dry debris, slab vs. loose type, and natural vs. artificial release for all included avalanche observations (Greene et al., 2016). In order to focus on dry slab avalanches we began by filtering out all wet and loose snow avalanches from these databases. To explore topographic effects on detection rates, we extracted: 'average elevation of the avalanche path', the 'average slope', 'average profile curvature', 'path length', and 'path width' (using a minimum bounding geometry on the paths from step 2.4) (Gesch et al., 2002). The Global Forest Cover Change Tree Cover Multi-Year Global Dataset (GFCC), i.e. the horizontal percentage of ground covered by woody vegetation greater than 5 meters in height in 2015, provided the average tree coverage within each avalanche path (Sexton et al., 2013). C-band SAR backscatter is heavily affected by tree cover, so we chose this variable to explore if tree cover in the debris zone negatively affected the detection rates (Vreugdenhil et al., 2018). Finally, we extracted the 'percentage of the path affected by radar layover effects' (phenomena that occur in steep topography due to the side-looking geometry of the SAR sensor), 'percentage affected by radar shadow' (no-data zones from lack of returning SAR energy), 'lag time' (the number of days between the avalanche's field observation and the acquisition of the activity image), and the 'average local incidence angle' (angle between the incoming microwave energy and the normal to the ground surface) within each avalanche path from the Sentinel-1 image pair (Table 2). Geometric terrain correction cannot unfold layover areas so that successful avalanche debris detection is limited in heavily affected regions.

Table 2: Explanatory Factors with data sources, spatial resolutions, and shortened names.

Explanatory Factor	**Source**	**Resolution**	**Alias**	**Range**
Destructive size of avalanche	BTAC, UDOT		D-size	1–4.5
Mean tree coverage percentage in the path	GFCC	30 m	Tree Perc	0–47%
Average elevation of avalanche path	USGS NED	10 m	Elevation	1857–3823 m
Average slope in the path	USGS NED	10 m	Slope Angle	15–55°
Avalanche path length	USGS NED	10 m	Path Length	0.19–3.2 km
Avalanche path width	USGS NED	10 m	Path Width	0.13–1.8 km
Average profile curvature in the path	USGS NED	10 m	Curvature	0–0.175
Average local incidence angle within the path	USGS NED, Sentinel-1	20 m	Incidence Angle	11–83°
Percentage of the path affected by radar layover	Sentinel-1	20 m	Layover Perc	0–77%
Percentage of the path affected by radar shadow	Sentinel-1	20 m	Shadow Perc	0–54%
Days between avalanche and the activity image acquisition	Sentinel-1	1 day	Lag Days	1–11

2.7 Statistical analysis

For our statistical analysis, we used the entire dataset of possible detections from all 14 image pairs. This resulted in 506 potential detections for the 258 field reported dry avalanche events. The increased number of possible detections relative to field reported avalanches is due to the combined effects of multiple opportunities to detect a unique event and the varying spatial footprint and temporal coverages of the different image pairs. The varying spatial and temporal footprints means that a single unique event could be included in one or more image pairs, hence resulting in a final dataset of 506 detectable avalanche events. Table 1 details the possible field reported avalanches that could have been detected in each pair of images. We calculated the

covariance of our quantitative variables using Spearman's rank correlation test (Wilks, 2019). If two variables were strongly correlated ($p < 0.05$ or $|r_s| > 0.5$), we retained the variable that appeared most directly in the conceptual model of avalanche debris backscatter (Eckerstorfer and Malnes, 2015). We also performed Shapiro Wilk's test for normality on all quantitative variables. All variables failed the test for normality.

We then identified explanatory variables with significant variance between the detected and undetected avalanches. We used thresholds of $p<0.05$ as significant and $p<0.1$ for marginally significant. Since all variables failed the test for normality, we performed the non-parametric equivalent of the Student t-test: the Mann Whitney U (MWU) test. We use the MWU to analyze if values from each explanatory variable from our detected avalanches were larger or smaller than values from our non-detected avalanches (Wilks, 2019).

We split the full dataset ($n = 506$) of potential detections into those appearing in either ascending or descending image pairs. We again used the MWU to compare detection rates, destructive size, and average local incidence angles between our different directions (Wilks, 2019).

Finally, we wanted to investigate the dataset for non-linear variable importance. Consequently, we trained a random forest model to identify detectable vs. non-detectable avalanches (Breiman, 2001). The random forest used the entire dataset of possible detections with 10-fold cross-validation ($n = 506$). Additionally, we inserted a random variable to assess which variables were more important than a random variable. We tuned the hyperparameter based on maximizing validation accuracy to optimize the number of decision trees (250) and the network's max depth (3). The random forest's performance was assessed with an accuracy score and F1 score, a

weighted average of precision and recall (Liu et al., 2014). We finished by extracting feature importance from the trained random forest.

3 Results

3.1 Image pairs and field location detection rates

Overall, we achieved a POD of 49% by successfully identifying 250 of our potential opportunities to detect avalanche debris and missing 256. This total set is larger than the 258 field observed avalanches, as a single avalanche can be observed, or not observed, in multiple temporally overlapping images. However, the detection rates varied between the two field locations and between image pairs.

The average POD of avalanches in the BTAC dataset was 41% and of avalanches in the UDOT dataset 57%. As mentioned earlier, the UDOT dataset contained multiple avalanche reports per path. Since we did not know which avalanche debris was detected in the Sentinel-1 images, all field-observed avalanches in a particular path were marked either as ‘detected’ or ‘not detected’. When extracting avalanche paths that had only one avalanche observation (N=48), the POD of this subset of single UDOT avalanches was 46%.

POD for individual image pairs for both regions ranged from 15% up to 86%. The number of avalanches in individual image pairs ranged from 18 to 47. There were significant differences between the two orbit directions of the image pairs. Ascending image pairs averaged a POD of 54%, while descending image pairs averaged 41% ($p = 0.0058$). There were also significantly higher incidence angles in ascending image pairs (53°) vs descending images (42°) pairs ($p < 0.0001$). Finally, the mean destructive size of the avalanches was also significantly higher ($p = 0.01$) in ascending images (2.3 vs 2.5). We extracted the following explanatory variables for

346 analysis of image pair variability further below: the number of avalanches, median destructive
347 size of avalanches, and the median local incidence angle (Table 3).

348 Table 3: Image Pairs with PODs. Darker colors show larger incidence angles or higher POD.

Site	Ref Date	Act Date	Direction	Orbit	# aval.	D-Size	Incidence Angle	Detection %
BTAC	1/24/18	2/5/18	Descending	100	19	2.0	36	21
BTAC	1/27/18	2/8/18	Ascending	49	31	2.5	50	52
BTAC	1/31/18	2/12/18	Descending	27	43	2.5	38	47
BTAC	1/2/20	1/14/20	Descending	100	41	2.0	32	20
BTAC	1/5/20	1/17/20	Ascending	49	28	2.0	51	39
BTAC	1/9/20	1/21/20	Descending	27	41	2.5	40	54
BTAC	1/10/20	1/22/20	Ascending	122	40	2.5	56	48
UDOT	12/22/19	1/3/20	Ascending	20	44	2.5	59	87
UDOT	12/28/19	1/9/20	Descending	27	18	2.5	50	50
UDOT	12/29/19	1/10/20	Ascending	122	42	2.5	51	52
UDOT	1/26/20	2/7/20	Descending	100	41	2.0	48	78
UDOT	1/27/20	2/8/20	Ascending	20	45	2.5	59	80
UDOT	2/2/20	2/14/20	Descending	27	26	2.5	50	15
UDOT	2/3/20	2/15/20	Ascending	122	47	2.5	51	19

349

350

351 ## 3.2 Covariation between explanatory variables for manual avalanche detection

352 We evaluated quantitative variable covariance with a Spearman's rank correlation test. Three
353 pairs of variables (Table 2) showed correlations over our threshold ($p < 0.05$ or $|r_s| > 0.5$): 1) the
354 'percentage of the path in shadow' with 'local incidence angle' ($r = 0.65$), 2) 'average elevation'
355 with 'tree percentage' ($r = 0.50$), and 3) 'path width' with 'path length '($r = 0.59$). For the first

pair we retained ‘path length’ due to its higher correlation with detection rates. For the second pair we retained ‘tree percentage’ also due to its higher correlation to detection rates.

For the ‘percentage of the path in shadow vs. local incidence angle’ – we retained ‘local incidence angle’ because the ‘percentage of path in shadow’ was less correlated to detection rates and had a seemingly nonintuitive sign of correlation. As the ‘percentage of the path in shadow’ increased, the detection rates also increased, which is not a logical trend for these two variables. However, when considering the positive relationship between higher incidences angle and detection rates this relationship between shadow percentage and detection rates is clarified. The higher incidence angles that led to increased detection rates would also lead to greater percentages of the path being affected by radar shadow.

3.3 Importance of explanatory variables on detection rates

We performed the non-parametric MWU tests on the full dataset and separate subsets for BTAC and UDOT regions since our variables were not normally distributed (please refer to supplementary material). The significant variables between our detected and undetected avalanches were generally the same between our full and regional datasets with ‘destructive size’, ‘incidence angle’, ‘path length’, and ‘lag days’ being the most important variables (

373 Table 4).

374

375

Table 4: Mann Whitney U test results for the full dataset, UDOT, BTAC. For all marginally significant or significant results, the detected and undetected median relative values are noted below the p-value. Darker green shows higher significance.

Variable	D-Size	Tree Perc	Incidence Angle	Slope	Curvature	Path Length	Layover Perc	Lag Days
Full Dataset								
p-value	7.3E-11	0.39	2.2E-05	0.0038	0.61	1.9E-16	0.97	2.5E-06
	det > undet		det > undet	det > undet		det > undet		det = undet
BTAC								
p-value	1.3E-13	0.76	0.0099	0.64	0.068	1.7E-07	0.15	0.43
	det > undet		det > undet			det > undet		
UDOT								
p-value	0.07	0.33	0.019	0.0052	0.032	3.4E-09	0.16	1.4E-05
			det > undet	det > undet	det < undet	det > undet		det < undet

For the four explanatory variables with significant variance, we show the difference between 'detected' and 'non detected' in Figure 5 for the entire dataset. Our individual regional datasets showed similar patters to the overall dataset. There is considerable overlap in the interquartile range for all explanatory variables with significantly higher medians for 'detected' vs 'non detected'.

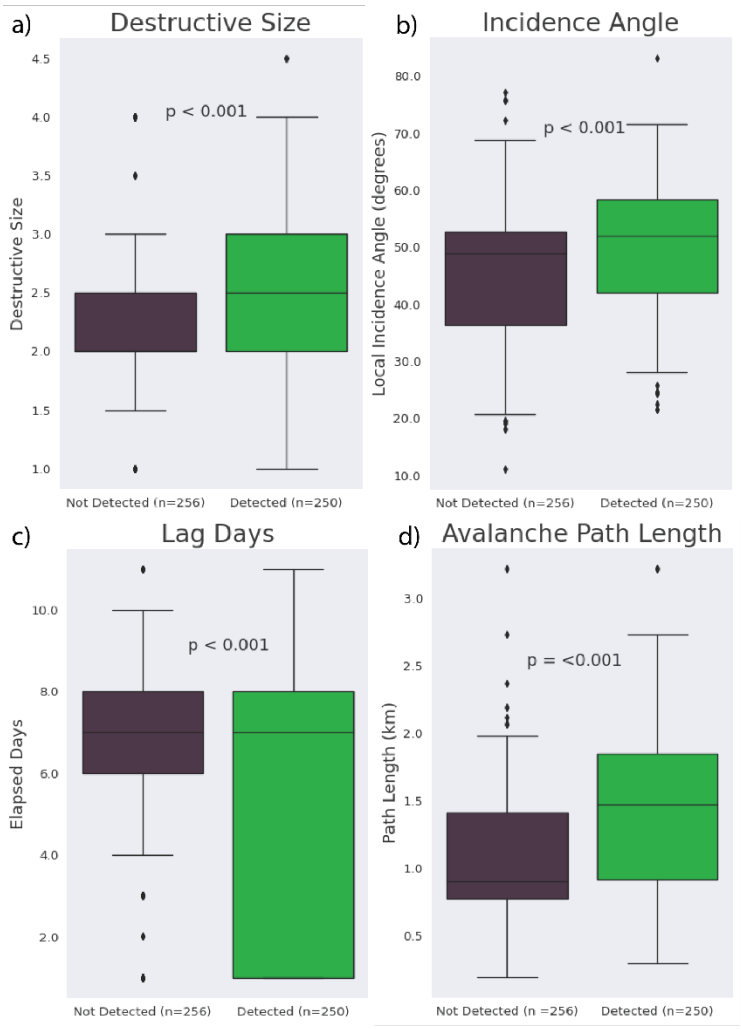

387

388 Figure 5: Boxplots showing the median, interquartile ranges, whiskers, and outliers for detected
389 and undetected avalanches in the full dataset. Whiskers extend to the last data point that is within
390 1.5 times the interquartile range above (below) the upper (lower) quartile, and outliers are data
391 points beyond that 1.5 times the interquartile range from the lower or upper quartile.

392

393 Previous research has established destructive size as a controlling variable on detection rate
394 (Eckerstorfer et al., 2019, Hafner et al. 2021). We also found a strong relationship between
395 increased POD and larger avalanches for the BTAC dataset and a marginal relationship for the
396 UDOT (Table 5). When we consider avalanches large enough to destroy trees or bury a car, or

larger (i.e., ≥ D3) we obtained a POD of 65% (n = 164). Those smaller than D3 had a POD of 42%.

Table 5: Detection rates by destructive size. Darker green represents higher detection rates. Bold horizontal line marks the threshold between smaller (<D3) from relatively larger avalanches (≥D3).

Destructive Size	# Detected	# Not	Detection Rate	
1	4	23	15%	
1.5	26	43	38%	
2	78	100	44%	< D3: 44%
2.5	60	47	56%	
3	56	41	58%	
3.5	17	2	89%	≥ D3: 65%
4	31	15	67%	
4.5	2	0	100%	

3.4 Random forest feature importance in detection rates

Following hyperparameter tuning, the random forest attained a validation accuracy of 64% with 10-fold cross-validation. The feature importance from the random forest results aligned with the findings from the MWU analysis with ‘path length’, ‘incidence angle’, ‘lag days’, and ‘destructive size’ as the most significant variables (Table 6).

412 Table 6: Feature individual and cumulative importance in the random forest model.

Feature	Individual Importance	Cumulative
Path Length	33%	33%
Lag Days	19%	52%
Incidence Angle	13%	65%
D- Size	12%	77%
Slope	6%	83%
Curvature	5%	88%
Tree Percentage	5%	93%
Layover Percentage	4%	97%
Random Variable	3%	100%

413

414 # 4 Discussion

415 ## 4.1 Manual avalanche detection using Sentinel-1 in a transitional snow climate

416 Our study is the first to provide a large-scale analysis of detection rates for Sentinel-1 images
417 relative to field observed datasets in the continental United States, which has a markedly
418 different topography and snow climate from previous SAR avalanche detection studies.
419 Our POD was 49% from two field locations utilizing SAR temporal change analysis on a dataset
420 of dry slab avalanches (with 248 unique avalanche events, and 506 opportunities to detect in the
421 images). However, when considering avalanches equal to or larger than D3 the manual detection
422 rate rises to 65%. SAR temporal change analysis is effective for most avalanches large enough to
423 do substantial damage to infrastructure or vegetation. However, we still miss around 35% of
424 even these large avalanches.
425 The detection rate for the UDOT avalanches (POD = 53%) is substantially higher than for the
426 BTAC avalanches (POD = 41%). Considering only UDOT avalanche paths with single events,

the detection rate dropped to 46%, thus much closer to the BTAC POD, suggesting fairly similar results. Both field locations are in a transitional snow climate where wet and dry snow avalanche cycles can be expected. However, the vast majority of observed avalanches were dry snow avalanches, which is the focus of this study.

Previous research on wet snow avalanches detected 100% of avalanches D3 and larger (Eckerstorfer et al., 2019). Our study, focused solely on dry snow avalanches, found a much lower detection rate (64%) for comparably sized avalanches. While there are topographic and climatic factors that may be influencing these results, our results suggest that a maritime snow climate dominated by wet snow avalanche activity may be better suited to Sentinel-1 temporal change analysis techniques.

4.1.1 How did detection rates vary between image pairs?

Detection rates differed between Sentinel-1 image pairs, with the lowest detection rate being 15% and the highest being 87% (Table 3). This means that certain pairs of images are more suitable for detecting avalanche debris than others. A trend in detection rates was that ascending image pairs had higher detection rates (54%) compared to descending image pairs (41%) ($p = 0.0058$). While there was a skew towards larger avalanches in ascending image pairs ($p = 0.01$) the difference in medians was only 0.5 and probably doesn't fully account for the observed differences in detection rates.

A more likely explanation for varying detection rates might be the trends in aspect of the active avalanche paths relative to the SAR sensor. Ascending image pairs had higher median incidence angles (53.2°) relative to descending image pairs (42.2°) ($p < 0.001$). In Wyoming and Utah, due

449 to prevailing wind direction and less solar warming, more avalanches are noted in field
450 observations on east facing aspects. This predominance of east facing avalanches means that in
451 ascending images, there were more paths that faced away from the sensor leading to higher
452 incidence angles and, based on this study and Tompkin and Leinss (2021), to higher detection
453 rates. Generally, this relationship suggests that depending on the predominant aspects of
454 avalanches in a region, either flight direction (ascending or descending), will yield higher
455 detection rates.
456

457 ## 4.2 Which explanatory factors correlated with successful detections?

458 Several explanatory factors reached high significance in our MWU tests for one or more of the
459 datasets. We present these explanatory factors in descending order of significance and the
460 associated reason for an increased detection rate in

461 Table 7. Then we discuss each of the explanatory factors separately below.

462

463

464 Table 7: Summary of explanatory factors related to increased detection rates sorted by Mann-
465 Whitney U (MWU) test p-values.

Explanatory factors	**Increased Detection Rates**	**MWU P-Value**	**RF Importance**
Path length	Longer path length	<0.001	1st
Lag Days	Fewer days elapsed	<0.001	2nd
Local incidence angle	Increased local incidence angles	<0.001	3rd
Destructive size	Larger destructive size	<0.001	4th
Slope angle	Steeper average slope angle	0.0038	6th
Curvature	More convex curvature	0.032 (UDOT only)	5th
Layover Percentage		>0.1	8th
Tree Coverage		>0.1	7th

466

467 4.2.1 Destructive size

468 Our results show a strong and positive correlation between the field reported destructive size and
469 Sentinel-1 based POD for our whole dataset and for the BTAC subset ($p<0.001$) (Table 5). The
470 marginal significance of destructive size in the UDOT dataset may have been due to overlapping
471 avalanches in paths causing increased detections of smaller avalanches that occurred
472 simultaneously with larger avalanches. This matches previous results reported by Eckerstorfer et
473 al. (2019) and Hafner et al. (2021). Both studies found PODs around 90–100% for D4 and D5
474 avalanches dropping off rapidly for smaller avalanches, with Hafner et al. (2021) reporting
475 detection rates of only 4% for D1s. Our results match this general trend, with a 29% detection
476 rate for avalanches D1.5, 47% for D2 to D2.5 and 65% for all D3 and larger. A probable
477 explanation for our lower detection rates of large avalanches is our dataset was only dry

avalanches, unlike the dataset in Eckerstorfer et al. (2019) that was over 90% wet avalanches and Hafner et al. (2021) that was composed of a mixture of dry and wet snow avalanches.

The correlation between destructive size and POD is likely due to the spatial resolution of the Sentinel-1 sensor. Larger avalanches will typically result in wider and deeper debris piles. These expanded debris piles are easier to detect with the relatively coarse resolution of the Sentinel-1 sensor. Leinss et al. (2020) suggested a smallest detectable size of 2000 m^2 for avalanche debris in their Sentinel-1 automated avalanche detection system, while Eckerstorfer et al. (2019) use a minimum cut-off size of 4000 m^2.

Avalanche inventories using Sentinel-1 are biased towards larger avalanches. Higher resolution sensors may improve the ability to detect smaller avalanches, as shown by Eckerstorfer and Malnes (2015) using very high resolution Radarsat-2 ultrafine data for avalanche detection. However, if infrastructure damage is the primary concern, accurate mapping of more significant avalanches with Sentinel-1 will be sufficient in most applications.

4.2.2 Avalanche type

Compared to previous studies, our results provide further supporting evidence that dry avalanches are more difficult to detect than wet avalanches. Our dataset was entirely dry avalanches and we consistently found lower POD rates than those in previous research on the detection rates for wet snow avalanches (Eckerstorfer et al. 2019, Hafner et al. 2021). Consequently, SAR-based avalanche detections may be best suited to regions dominated by wet snow avalanches. An overall lower POD can be expected in transitional or continental snow climates.

Dry snow is mostly transparent for C-band SAR, which means that an unknown contribution from the ground surface can be expected to the total backscatter signal. This results in minor relative backscatter difference between avalanche debris and surrounding undisturbed snow in dry snow conditions. In case of wet snow avalanches, the SAR signal does not penetrate the snow, leading to the majority of the backscatter signal stemming from the air-surface interface, that is typically rough in wet snow avalanches. A major difference in backscatter between the debris and the surrounding snow can thus be expected, which is more likely detectable in wet snow than in the case of dry snow.

4.2.3 Path length

Previous studies have not investigated the relationship between detection rates and 'path length'. We found a strong relationship (MWU p-value <0.001 and first in the random forest feature importance), with longer paths having higher detection rates. Intuitively, longer paths may produce larger avalanches. However, we did not find path length to be significantly correlated with destructive size, suggesting that path morphology rather than total mass of the avalanche is more important. Future research is needed to confirm our findings, but our study suggests that certain regions with longer path lengths might lead to higher detection rates.

4.2.4 Local incidence angle

The average local incidence angle was significant in the MWU comparisons for every dataset ($p<0.02$, Table 4) and was the second most important feature in our random forest model (Table 6). This relationship between high local incidence angle and high detection rates is based on a

few factors. First, due to the geometry of SAR images there is higher resolution in areas where the incidence angle is farther from zero. Also, this limits the effects of layover, which can obscure avalanche debris. This result matches the findings of Tompkin and Leinss (2021) whose work with exclusively wet snow avalanches showed a 4 dB increase in avalanche debris backscatter change for incidence angles between 40–70° for VV polarization and 2 dB for VH polarization. (Figure 6).

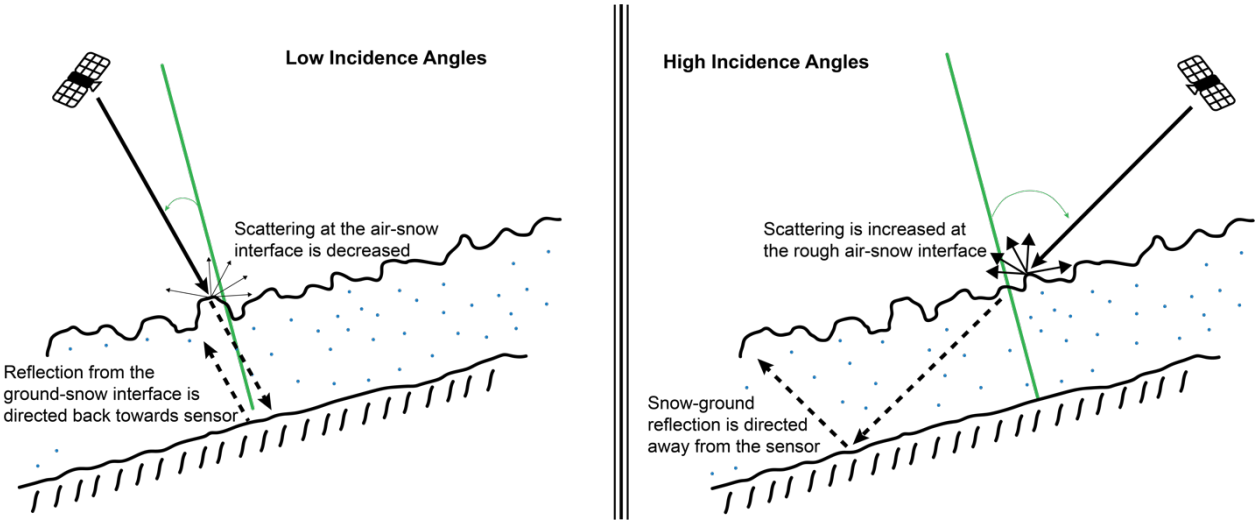

Figure 6: Proposed conceptual model explaining the increased detection rates of avalanche debris at higher incidence angles.

Future applications could also use this knowledge to differentiate paths with a high chance of detecting avalanches from those with a relatively low probability. Identifying paths with a high POD is valuable for suggesting when avalanches are not occurring instead of just being missed by this technique.

4.2.5 Lag days

539 The elapsed days between the avalanche field observation and the acquisition of the Sentinel-1
540 activity image was highly significant for our complete and UDOT datasets ($p<0.001$, Table 4),
541 with fewer lag days correlated with higher detections. The median lag days for detected
542 avalanches in the UDOT dataset was 2 compared to 8 for the undetected UDOT avalanches.
543 Additionally, it was the 3rd most important variable in our random forest.
544 This connection between fewer days elapsed and higher detection rates makes intuitive sense.
545 The increased number of days leads to greater exposure to ablative meteorological factors such
546 as: 1) increased temperatures that might reduce the chances of detection due to melting and
547 smoothing of the rough avalanche surface, 2) increased cumulative precipitation, which might
548 cover the rough surface of the debris and lead to a less dramatic contrast between the increased
549 volumetric backscatter from the deeper avalanche debris and the surrounding snowpack, and 3)
550 more exposure to wind redistribution, which might smooth the avalanche debris surface. In
551 regions with less frequent Sentinel-1 imaging or high repeat frequencies (such as lower latitudes
552 and outside of Europe), atmospheric weathering will likely cause lower detection rates.
553 It is unclear why the BTAC did not have a significant effect from lag days. Potentially the
554 atmospheric conditions of Little Cottonwood Canyon, Utah (generally warmer and less frequent
555 intense storms) lead to greater reductions in detectability relative to Wyoming (generally more
556 continually snowy, colder average temperatures) for these cycles. Future research into the
557 specific meteorological conditions that lead to lower PODs with increased days of exposure may
558 be valuable for understanding these underlying causes.
559
560 4.2.6 Layover percentage

The percentage of the path affected by layover did not result in significant MWU results ($p = 0.42$, Table 4) and was only slightly more important than a random variable in our random forest. Thus, our results do not provide evidence for a connection between layover effect and detection rates. However, layover can effectively obscure large portions of an avalanche path, leading to missed detections. Therefore, the conclusion that paths highly affected by layover would have lower detection rates seems reasonable. While this study did not find evidence for a relationship between layover and detection rates, we did note a few outliers, where layover did impact detection. The low significance of layover on detection rates may have been because our sample only had a median layover percentage of 3% suggesting that our paths may have had limited impacts from layover.

4.2.7 Avalanche slope angle

The average slope (across the entire path) was significant in the overall and UDOT dataset ($p = 0.0038$, Table 4) and the fifth most important feature in our random forest (Table 6). The median slope was 33 degrees for detected avalanches and 31 degrees for the undetected avalanches. These results suggest a slight relationship between steeper slopes and higher detection rates but may also be due to steeper slopes generally having higher incidence angles in this study. The weaker relationship between slope and POD for the BTAC may be explained by the relatively larger spatial extent of the avalanche observations in the BTAC dataset, rather than the single, steep canyon for the UDOT data.

4.4 Limitations and future work

583 This study assessed the detectability of avalanches in Sentinel-1 images in a transitional snow
584 climate in the United States. We noted several limitations that may help guide future research:

585 1) Our avalanches datasets covered only two regions of a similar snow climate. Expanding
586 to other regions within the transitional snow climate, as well as purely continental or
587 maritime snow climates in the United States would be useful. An excellent potential
588 study area would be Alaska, which receives more Sentinel-1 overflights, reducing lag
589 days and thus atmospheric influence on avalanche debris. The coastal climate and large-
590 scale topography with long avalanche paths in Alaska may also improve avalanche
591 detectability.

592 2) This research utilized only four avalanche cycles with 258 field reported avalanches,
593 resulting in 506 potentially detections of avalanches in our SAR images. These four
594 avalanche cycles were selected to maximize the number of avalanches in each pair of
595 Sentinel-1 images but choosing events from these extreme avalanche cycles may have
596 introduced other factors that skewed our results (e.g. more long runouts). Studies in the
597 future with additional avalanche cycles may help to clarify if our findings hold for less
598 extreme avalanche cycles. Additionally, exploring spring avalanche cycles will be
599 valuable, considering also wet snow avalanche activity.

600 3) We utilized avalanche records that were opportunistically collected. The BTAC records
601 may have been incorrect due to non-expert public sources reporting. These records were
602 potentially also skewed towards accessible locations, periods of high visibility, and larger
603 events. Future studies could limit these biasing effects by performing randomized
604 observations or confirming complete coverage of a region.

4) We focused exclusively on backscatter analysis of a single sensor. Future studies could explore other SAR sensors for avalanche detection, operating at different frequencies (e.g. X-band) and spatial resolutions.
5) We carried out manual detections, which are currently considered the gold standard of avalanche detection using SAR imagery (Bianchi et al., 2021). However, since only one person (the first author) performed the manual detections, there may have been biases that systematically or randomly affected the results. Future studies may want to compare multiple people independently detecting avalanche debris in SAR image to explore the variability of expert interpretation.
6) Our techniques relied on manual detection but monitoring seasonal avalanche activity or a larger dataset of avalanche cycles will require automatic detection methods. Currently, classification of SAR images using neural networks shows promising results (Tompkin and Leinss, 2021, Bianchi et al., 2021). Future research combining these manual detections with machine learning techniques to explore automatic detections of dry snow avalanches will be valuable. This future machine learning work would also benefit from the establishment of a community-recognized dataset of manual detections and imagery to test new models against. This study and others have shown the wide range in site and event-specific PODs, so improvements in model performance are only meaningful if done against a common set of images and detections.
7) While we assessed whether a single manual observer could use SAR imagery to detect an avalanche that had been observed in the field (our Probability of Detection or POD), we did not assess how often that manual observer might have identified an avalanche that did

not occur in the field (the false alarm rate or FAR). Doing this requires the observer to start with SAR imagery with no knowledge of avalanche activity, and then to identify all areas that appear to be avalanche debris. It would also require a spatially and temporally complete data set of avalanche activity for the area, which was unavailable to us. Obtaining such datasets is critically important for furthering this research because quantifying this manual FAR is critical to provide context for automating future avalanche detection, which often relies on manually labeled training data.

5 Conclusion

This study examined the manual avalanche detection rates in Sentinel-1 backscatter intensity data relative to datasets of field observed dry snow avalanches from two locations in a transitional snow climate in the western United States. For the 506 potentially observable avalanche events in the SAR images, 250 (49%) were manually detectable in the Sentinel-1 images, which were derived from the 248-field observed unique events examined in this study. This POD increased to 65% when considering only avalanches large enough to bury cars or break trees (≥D3). Thus, most dry snow avalanches larger than D3 can be detected by SAR-based change detection analysis, though this technique still missed about 35% of these avalanches in our combined database.

The primary variables showing a strong correlation with detection rates (both in our MWU and random forest analysis) are local incidence angle, path length, destructive size, slope angle, and elapsed days between the avalanche and the activity image. We also established a much weaker, and statistically insignificant relationship for the percentage of path affected by layover. Tree

coverage, average slope steepness, and the slope's curvature failed to reach a marginal significance.

With further refinements, our methods may provide a first step toward automated avalanche detection using remote sensing. This, in turn, would give avalanche practitioners in the United States much-needed feedback and researchers spatially extensive and relatively complete datasets of avalanche occurrences for machine learning techniques and trend analysis. Though the lower latitudes of the United States only have revisit intervals of ~2–4 days instead of the daily revisit interval near the poles, there is still reasonable temporal coverage for detection of major avalanche events in a reasonably timely manner. Within the United States there are specific regions, in particular Alaska, that may be better suited to immediate applications of this technology including manual mapping of major cycles and automated near-real time detection techniques.

ACKNOWLEDGEMENTS

We would like Peter Gauer and our two anonymous reviewers for their comments which greatly improved the writing and content of this manuscript. We are also grateful to the European Space Agency for providing Sentinel-1 data.

References

Abermann, J., Eckerstorfer, M., Malnes, E., Hansen, B.U., 2019. A large wet snow avalanche cycle in West Greenland quantified using remote sensing and in situ observations. Nat Hazards 97, 517–534. https://doi.org/10.1007/s11069-019-03655-8

Bianchi, F.M., Grahn, J., Eckerstorfer, M., Malnes, E., Vickers, H., 2021. Snow avalanche segmentation in SAR images with Fully Convolutional Neural Networks. IEEE Journal of Selected Topics in Applied Earth Observations and Remote Sensing 14, 75–82. https://doi.org/10.1109/JSTARS.2020.3036914

Birkeland, K., 2017. In Response to Avalanche Fatalities in the United States by Jekich et al. Wilderness and Environmental Medicine 28. https://doi.org/10.1016/j.wem.2017.06.009

Breiman, L., 2001. Random Forests. Machine Learning 45, 5–32. https://doi.org/10.1023/A:1010933404324

Eckerstorfer, M., Bühler, Y., Frauenfelder, R., Malnes, E., 2016. Remote sensing of snow avalanches: Recent advances, potential, and limitations. Cold Regions Science and Technology 121, 126–140. https://doi.org/10.1016/j.coldregions.2015.11.001

Eckerstorfer, M., Malnes, E., 2015. Manual detection of snow avalanche debris using high-resolution Radarsat-2 SAR images. Cold Regions Science and Technology 120, 205–218. https://doi.org/10.1016/j.coldregions.2015.08.016

Eckerstorfer, M., Vickers, H., Malnes, E., Grahn, J., 2019. Near-Real Time Automatic Snow Avalanche Activity Monitoring System Using Sentinel-1 SAR Data in Norway. Remote Sensing 11, 2863. https://doi.org/10.3390/rs11232863

Gaume, J., van Herwijnen, A., Chambon, G., Wever, N., Schweizer, J., 2017. Snow fracture in relation to slab avalanche release: critical state for the onset of crack propagation. The Cryosphere 11, 217–228. https://doi.org/10.5194/tc-11-217-2017

Gesch, D., Oimoen, M., Greenlee, S., Nelson, C., Steuck, M., Tyler, D., 2002. The National Elevation Dataset. Photogrammetric Engineering and Remote Sensing 68, 5–11.

Gorelick, N., Hancher, M., Dixon, M., Ilyushchenko, S., Thau, D., Moore, R., 2017. Google Earth Engine: Planetary-scale geospatial analysis for everyone. Remote Sensing of Environment, Big Remotely Sensed Data: tools, applications and experiences 202, 18–27. https://doi.org/10.1016/j.rse.2017.06.031

Greene, E., Birkeland, K., Elder, K., Mccammon, I., Staples, M., Sharaf, D., 2016. Snow, Weather, and Avalanches: Observational Guidelines for Avalanche Programs in the United States, 3rd ed. American Avalanche Association, Victor, ID.

Hafner, E., Techel, F., Leinss, S., Bühler, Y., 2021. Mapping avalanches with satellites - evaluation of performance and completeness. The Cryosphere 15, 983-1004. https://doi.org/10.5194/tc-983-2021

Hendrikx, J., Murphy, M., Onslow, T., 2015. Classification trees as a tool for operational avalanche forecasting on the Seward Highway, Alaska. Cold Regions Science and Technology 97, 113-120. https://doi.org/10.1016/j.coldregions.2013.08.009

Larsen, H., Hendrikx, J., Slåtten, M.S., Engeset, R.V., 2020. Developing nationwide avalanche terrain maps for Norway. Nat Hazards 103, 2829–2847. https://doi.org/10.1007/s11069-020-04104-7

Leinss, S., Wicki, R., Holenstein, S., Baffelli, S., Bühler, Y., 2020. Snow avalanche detection and mapping in multitemporal and multiorbital radar images from TerraSAR-X and Sentinel-1. Natural Hazards and Earth System Sciences 20, 1783–1803. https://doi.org/10.5194/nhess-20-1783-2020

Liu, Y., Zhou, Y., Wen, S., Tang, C., 2014. A Strategy on Selecting Performance Metrics for Classifier Evaluation. International Journal of Mobile Computing and Multimedia Communications 6, 20–35. https://doi.org/10.4018/IJMCMC.2014100102

Malnes, E., Eckerstorfer, M., Larsen, Y., Frauenfelder, R., Jonsson, A., Jaedicke, C., Solbø, S., 2013. Remote sensing of avalanches in northern Norway using Synthetic Aperture Radar. Presented at the International Snow Science Workshop, Grenoble, France. https://doi.org/10.13140/2.1.2462.0481

McClung, D.M., 2002a. The Elements of Applied Avalanche Forecasting, Part I: The Human Issues. Natural Hazards 26, 111–129. https://doi.org/10.1023/A:1015665432221

McClung, D.M., 2002b. The Elements of Applied Avalanche Forecasting, Part II: The Physical Issues and the Rules of Applied Avalanche Forecasting. Natural Hazards 26, 131–146. https://doi.org/10.1023/A:1015604600361

McClung, D.M., Schaerer, P., 2006. The Avalanche Handbook. The Mountaineers.

Mears, A., 1992. Snow-avalanche hazard analysis for land-use planning and engineering, Bulletin (Colorado Geological Survey). Colorado Geological Survey, Dept. of Natural Resources, Denver, Colorado.

Mock, C., Birkeland, K., 2000. Snow Avalanche Climatology of the Western United States Mountain Ranges. Bulletin of the American Meteorological Society 81(10), 2367-2392. https://doi.org/10.1175/1520-0477(2000)081<2367:SACOTW>2.3.CO;2

Schweizer, J., Kronholm, K., Wiesinger, T. 2003. Verification of regional snowpack stability and avalanche danger, Cold Regions Science and Technology 37, 277-299. https://doi.org/10.1016/S0165-232X(03)00070-3

Sexton, J., Song, X.-P., Feng, M., Noojipady, P., Anand, A., Huang, C., Kim, D.-H., Collins, K., Channan, S., Dimiceli, C., Townshend, J., 2013. Global, 30-m resolution continuous fields of tree cover: Landsat-based rescaling of MODIS vegetation continuous fields with lidar-based estimates of error. International Journal of Digital Earth 6, 1–22. https://doi.org/10.1080/17538947.2013.786146

Tompkin, C., Leinss, S., 2021. Backscatter Characteristics of Snow Avalanches for Mapping with Local Resolution Weighting. IEEE Journal of Selected Topics in Applied Earth Observations and Remote Sensing 14, 4452-4464. https://doi.org/10.1109/JSTARS.2021.3074418

Vollrath, A., Mullissa, A., Reiche, J., 2020. Angular-Based Radiometric Slope Correction for Sentinel-1 on Google Earth Engine. Remote Sens 12, 1867.

Vreugdenhil, M., Wagner, W., Bauer-Marschallinger, B., Pfeil, I. 2018. Sensitivity of Sentinel-1 Backscatter to Vegetation Dynamics: An Australian Case Study. Remote Sens 10, 1396. https://doi.org/10.3390/rs10091396.

Wiesmann, A., Wegmuller, U., Honikel, M., Strozzi, T., Werner, C.L., 2001. Potential and methodology of satellite based SAR for hazard mapping, in: IGARSS 2001. Scanning the Present and Resolving the Future. Proceedings. IEEE 2001 International Geoscience and Remote Sensing Symposium (Cat. No.01CH37217). Presented at the IGARSS 2001.

752 Scanning the Present and Resolving the Future. Proceedings. IEEE 2001 International
753 Geoscience and Remote Sensing Symposium (Cat. No.01CH37217), pp. 3262–3264
754 vol.7. https://doi.org/10.1109/IGARSS.2001.978322
755 Wilks, D., 2019. Statistical Methods in the Atmospheric Sciences. Elsevier.
756 https://doi.org/10.1016/C2017-0-03921-6
757 Wynne, R., Campbell, J., 2011. Introduction to Remote Sensing, 5th ed. The Guilford Press.
758 Yang, J., Li, C., Li, L., Ding, J., Zhang, R., Han, T., Liu, Y., 2020. Automatic Detection of
759 Regional Snow Avalanches with Scattering and Interference of C-band SAR Data.
760 Remote Sensing 12, 2781. https://doi.org/10.3390/rs12172781
761